

UC Berkeley

UC Berkeley Previously Published Works

Title

Constraints on mantle viscosity and Laurentide ice sheet evolution from pluvial paleolake shorelines in the western United States

Permalink

<https://escholarship.org/uc/item/5vn6d215>

Authors

Austermann, J
Chen, CY
Lau, HCP
[et al.](#)

Publication Date

2020-02-01

DOI

10.1016/j.epsl.2019.116006

Peer reviewed

Journal Pre-proof

Constraints on mantle viscosity and Laurentide ice sheet evolution from pluvial paleolake shorelines in the western United States

J. Austermann, C.Y. Chen, H.C.P. Lau, A.C. Maloof, K. Latychev

PII: S0012-821X(19)30698-3

DOI: <https://doi.org/10.1016/j.epsl.2019.116006>

Reference: EPSL 116006

To appear in: *Earth and Planetary Science Letters*

Received date: 11 May 2019

Revised date: 26 November 2019

Accepted date: 3 December 2019



Please cite this article as: Austermann, J., et al. Constraints on mantle viscosity and Laurentide ice sheet evolution from pluvial paleolake shorelines in the western United States. *Earth Planet. Sci. Lett.* (2019), 116006, doi: <https://doi.org/10.1016/j.epsl.2019.116006>.

This is a PDF file of an article that has undergone enhancements after acceptance, such as the addition of a cover page and metadata, and formatting for readability, but it is not yet the definitive version of record. This version will undergo additional copyediting, typesetting and review before it is published in its final form, but we are providing this version to give early visibility of the article. Please note that, during the production process, errors may be discovered which could affect the content, and all legal disclaimers that apply to the journal pertain.

© 2019 Published by Elsevier.

Highlights

- Paleoshorelines of Lake Bonneville and Lahontan in the western U.S. are deformed.
- Deformation due to lake load implies low viscosity and thin elastic lithosphere.
- Lake load corrected shorelines exhibit northward dipping trend.
- Trend is caused by peripheral bulge associated with the Laurentide ice sheet.
- Trend implies low viscosity and constrains shape of Laurentide ice sheet.

1 **Constraints on mantle viscosity and Laurentide ice sheet evolution from pluvial**
2 **paleolake shorelines in the western United States**

3

4 J. Austermann^{1*}, C.Y. Chen^{2,3}, H.C.P. Lau⁴, A.C. Maloof⁵, K. Latychev^{1,6}

5

6 ¹ Lamont Doherty Earth Observatory, Columbia University, Palisades, NY 10964, USA

7 ² Massachusetts Institute of Technology-Woods Hole Oceanographic Institution Joint Program,
8 Cambridge, MA, 02139, USA

9 ³ Department of Earth, Atmospheric and Planetary Sciences, Massachusetts Institute of
10 Technology, Cambridge, MA, 02139, USA

11 ⁴ Earth and Planetary Science, University of California, Berkeley, CA 94720, USA

12 ⁵ Department of Geosciences, Princeton University, Guyot Hall, Washington Road, Princeton,
13 NJ 08544, USA

14 ⁶ Department of Earth and Planetary Sciences, Harvard University, Cambridge, MA 02138, USA

15 * corresponding author, jackya@ldeo.columbia.edu

16

17 Keywords: Lake Bonneville, Lake Lahontan, paleoshorelines, glacial isostatic adjustment,
18 mantle viscosity, Laurentide ice sheet

19

20

21

22 **Abstract**

23 The deformation pattern of the paleoshorelines of extinct Lake Bonneville were among the first
24 features to indicate that Earth's interior responds viscoelastically to changes in surface loads
25 (Gilbert, 1885). Here we revisit and extend this classic study of isostatic rebound with updated
26 lake chronologies for Lake Bonneville and Lake Lahontan as well as revised elevation datasets
27 of shoreline features. The first order domal pattern in the shoreline elevations can be explained
28 by rebound associated with the removal of the lake load. We employ an iterative scheme to
29 calculate the viscoelastic lake rebound, which accounts for the deformation of the solid Earth
30 and gravity field, to calculate a lake load that is consistent with the load-deformed
31 paleotopography. We find that the domal deformation requires a regional Earth structure that
32 exhibits a thin elastic thickness of the lithosphere (15–25 km) and low sublithospheric Maxwell
33 viscosity ($\sim 10^{19}$ Pa s). After correcting for rebound due to the lake load, shoreline feature
34 elevations reveal a statistically significant northward dipping trend. We attribute this trend to
35 continent-scale deformation caused by the ice peripheral bulge of the Laurentide ice sheet, and
36 take advantage of the position of these lakes on the distal flank of the peripheral bulge to
37 provide new insights on mantle viscosity and Laurentide ice sheet reconstructions. We perform
38 ice loading calculations to quantify the deformation of the solid Earth, gravity field, and rotation
39 axis that is caused by the growth and demise of the Laurentide ice sheet. We test three different
40 ice reconstructions paired with a suite of viscosity profiles and confirm that the revealed trend
41 can be explained by deformation associated with the Laurentide ice sheet when low viscosities
42 below the asthenosphere are adopted. We obtain best fits to shoreline data using ice models
43 that do not have the majority of ice in the eastern sectors of the Laurentide ice sheet, with the
44 caveat that this result can be affected by lateral variations in viscosity. We show that pluvial
45 lakes in the western United States can place valuable constraints on the Laurentide ice sheet,
46 the shape of its peripheral bulge, and underlying mantle viscosity.

47

48 1. Introduction

49 The western U.S. experienced a mean increase in precipitation during the last glacial cycle,
50 which led to the formation of a series of pluvial lakes that filled the Basin and Range Province
51 (e.g., Benson et al., 1990; Mifflin and Wheat, 1971). The most prominent of those is Lake
52 Bonneville (30–10 ka), an extinct pluvial lake that occupied the eastern Great Basin (Fig. 1B). At
53 its maximum extent (~18 ka) (Oviatt, 2015), the lake had a volume of around 10,300 km³ (Chen
54 and Maloof, 2017), comparable to present-day Lake Superior. A significant portion of the lake
55 drained out of Red Rock Pass around 18 ka, and the remainder formed the Provo lake stage,
56 which lasted until about 15 ka (Oviatt, 2015) (Fig. 1B). What now remains of Lake Bonneville is
57 the Great Salt Lake in Utah. During Lake Bonneville's existence, the smaller Lake Lahontan
58 (Fig. 1C) occupied the western part of the Great Basin and experienced a similar increase and
59 decrease in lake volume, reaching its maximum extent at ca. 16–15 ka (Benson et al., 2013;
60 Reheis et al., 2014) (Fig. 1A).

61
62 Water stored in the basin during the occupation of these paleolakes exerted pressure on the
63 lithosphere and mantle causing downward deflection of Earth's surface. During these times,
64 shoreline features demarcating the lake surface formed on the landscape. After the lakes
65 drained, the solid Earth rebounded, pushing up shoreline features that formed on islands within
66 the deepest part of the lake to elevations higher than those at the lake's margin. Due to this
67 differential uplift in response to the lake unloading, shoreline features at the lake's center are
68 today significantly higher than those on its periphery (Fig. 1D-F). This pattern is most apparent
69 for features of the Bonneville lake stage, where differences in shoreline feature elevations are
70 over 70 m (Fig. 1E). These paleoshorelines have played an instrumental role in the
71 understanding of isostatic rebound on Earth. Gilbert (1885) reported this phenomenon and
72 provided several possible explanations including isostatic adjustment to the lake load and
73 changes in the gravitational equipotential surface due to load redistributions. While the latter are

74 small (Woodward, 1888), this early assessment paved the way for a gravitationally self-
75 consistent rebound theory that is used in ice age sea level calculations today (Whitehouse,
76 2018).

77

78 The amount of deflection of Lake Bonneville shorelines has been used in numerous studies to
79 constrain Earth's local viscoelastic properties (Bills and May, 1987; Cathles, 1975; Crittenden,
80 1963; Iwasaki and Matsu'ura, 1982; Nakiboglu and Lambeck, 1982; Passey, 1981). Most
81 recently, Bills et al. (1994) performed an inversion for a multilayer viscosity model and a fixed
82 lake load history resulting in a viscosity profile that exhibits a very low viscosity channel (4×10^{17}
83 Pa s) beneath the lithosphere that increases to 2.5×10^{20} Pa s at a depth of 150 km. The
84 lithosphere consists of a thin high viscosity layer (2×10^{24} Pa s from 0 to 10 km depth) followed
85 by an intermediate layer ($\sim 5 \times 10^{20}$ Pa s from 10 to 40 km depth). The rebound pattern of Lake
86 Lahontan was recognized significantly later than that of Lake Bonneville (Mifflin and Wheat,
87 1971), likely due to its smaller magnitude, with differences in shoreline feature elevations of only
88 up to 25 m (Fig. 1D). Adams et al. (1999) investigated the shoreline feature elevations, and Bills
89 et al. (2007) used them together with a fixed lake load history to identify a very low
90 sublithospheric viscosity (less than 10^{18} Pa s between 80–160 km). This minimum viscosity is
91 comparable to the values obtained for the Lake Bonneville region but might extend over a larger
92 depth range (Bills et al., 2007). Post-seismic studies from Lake Lahontan find slightly lower
93 viscosities over the same depth range but overlap within uncertainty with the lake rebound
94 obtained viscosities (Dickinson et al., 2016).

95

96 These Basin and Range sub-lithospheric viscosity estimates are significantly lower than global
97 average estimates at this depth of $\sim 5 \times 10^{20}$ Pa s, obtained from observations derived from
98 postglacial rebound (Peltier et al., 2015). Both Bonneville and Lahontan lie within the Basin and
99 Range Province, which formed as a result of extension-related faulting (Sonder and Jones,

100 1999). Joint inversions of seismic and petrologic studies indicate that this region is
101 characterized by a thin crust (30–35 km), shallow lithosphere-asthenosphere boundary (50–55
102 km), and a high asthenospheric potential temperature of 1525 °C (Lekić and Fischer, 2014;
103 Plank and Forsyth, 2016). These elevated sublithospheric temperatures are consistent with
104 body wave tomography results that reveal relatively high S- and P-wave speeds and a high P to
105 S-wave speed ratio, which suggests the presence of sublithospheric melt (Schmandt and
106 Humphreys, 2010). The low viscosity estimates derived from lake rebound studies is therefore
107 consistent with the notion that Earth structure underneath the Western U.S. is significantly
108 weaker than cratonic sites such as the Canadian and Fennoscandian shields from which
109 rebound-based estimates of viscosity are normally obtained (Lau et al., 2018).

110

111 Even after the lake rebound signal is corrected for, longer wavelength spatial trends in shoreline
112 elevations remain. For Lake Bonneville, this residual has largely been attributed to tectonic and
113 crustal deformation such as displacement along the tectonically active Wasatch fault, which
114 straddles the eastern flank of the paleolake (Bills et al., 1994; Nakiboglu and Lambeck, 1982).
115 Similarly, a northward dipping trend in the residual Lake Lahontan shorelines has been linked to
116 tectonics associated with the Yellowstone hot spot (Bills et al., 2007). An alternative explanation
117 put forth earlier by Bills and May (1987) explained a possible northward dipping trend in the
118 residual shoreline of Lake Bonneville with the lake's location on the peripheral bulge of the
119 Laurentide ice sheet. Postglacial rebound calculations of the North American peripheral bulge
120 place these western U.S. lakes on the ice-distal side of the bulge. This long wavelength trend in
121 topography is sampled by these much smaller lakes (Fig. 2A), resulting in paleoshoreline
122 features that are expected to dip downward towards the ice sheet (Fig. 2B). In addition to solid
123 Earth deformation, the Laurentide ice sheet also deforms the gravity field, exerting a
124 gravitational pull on water in the lake. This effect by itself would cause an upward dip (towards

125 the ice sheet) in paleoshoreline features, counteracting to some extent the downward dipping
126 signal associated with the solid Earth (Fig. 2B).

127

128 In this study, we revisit this classic rebound problem to investigate the putative northward
129 dipping trend in the paleolake shoreline features of Lake Lahontan and Lake Bonneville. We use
130 revised shoreline feature elevations and updated chronologies of lake level histories together
131 with state-of-the-art isostatic adjustment modeling to test the hypothesis that a statistically
132 significant northward dipping trend can be detected in all lake stages once the lake rebound
133 pattern is corrected for. We further use three different ice sheet reconstructions together with an
134 ice age sea level calculation to investigate which ice sheet—mantle viscosity structure
135 combination best reproduces the observed lake tilt. While proglacial lakes have been used to
136 constrain ice sheet evolution and mantle viscosity in recent work (Gowan et al., 2016; Lambeck
137 et al., 2017), this study is the first to investigate the deformation of distant pluvial lake
138 shorelines.

139

140

141 **2. Observations**

142

143 2.1 Lake chronology

144 Lake Bonneville and Lake Lahontan were the two largest pluvial lakes in the Great Basin during
145 the last Pleistocene glaciation (~30–10 ka; Fig. 1C). A common misconception is that these
146 lakes were hydrographically connected to the Laurentide or Cordilleran ice sheets as ice-
147 dammed or glacial lakes; in actuality, these lakes were hydrographically distinct and instead fed
148 by local precipitation and snowmelt delivered by perennial rivers (Reheis et al., 2014). Both
149 lakes occupied basins of similar topographic characteristics, filling in broad and flat valley floors
150 surrounded by steep mountainsides consistent with the extensional tectonic regime of the Basin

151 and Range Province. Although both lakes were essentially contemporaneous, the lake level
152 history of Lake Bonneville is better constrained. Lake Bonneville was a deeper lake existing as a
153 single entity over a greater period of its history. Thus, a reconstruction of its lake level history
154 that is consistent with most interpretations of sediment core and outcrop evidence has been
155 more feasible. In contrast, the shallower Lake Lahontan existed as several smaller,
156 disconnected sub-basins for most of its history, complicating attempts to reach consensus on its
157 lake level history (Benson et al., 2013; Bills et al., 2007; Reheis et al., 2014).

158

159 Figs 1A and 1B depict the most recent reconstructions of lake level histories for Lake Lahontan
160 and Lake Bonneville, respectively. Both histories were derived from many decades of extensive
161 field and sediment core observations and are constrained by hundreds of radiometric dates on
162 organic material, tufas, and tephras extracted from cores, exposed outcrops of lake deposits,
163 and deposits associated with geomorphic shoreline features (e.g., Adams et al., 1999; Briggs et
164 al., 2005; Oviatt, 1997; Oviatt et al., 1992; Patrickson et al., 2010; Sack, 2015; Spencer et al.,
165 2015). During their existence, each lake experienced a rise (transgression) and fall (regression)
166 of water level, and in certain instances, left behind evidence of their evolution in the form of
167 prominent shorelines features. Of the many sequences of paleoshorelines available, the
168 shoreline features most relevant to this study are those associated with the maximum extent of
169 Lake Lahontan, the Seho lake stage (~15 ka; Figs 1A and D), and the Bonneville and Provo
170 lake stages of Lake Bonneville (18 ka and 18–15 ka; Figs 1B, E and F). Evidence suggests that
171 Lake Bonneville did not occupy its maximum extent, the Bonneville lake stage, for more than a
172 few hundred years (Gilbert, 1885; Oviatt and Jewell, 2016) before a catastrophic collapse of an
173 alluvial-fan dam dropped lake levels by 100 m to settle at the Provo level (Miller et al., 2013).

174

175 For clarity and simplicity, we hereafter use *Seho* in reference to the stage at which Lake
176 Lahontan reached its greatest extent (e.g., the Seho shoreline or Seho lake stage), and

177 *Bonneville* and *Provo* in reference those stages associated with Lake Bonneville's history (e.g.,
178 the Bonneville shoreline or Provo lake stage). The phrases *Lake Lahontan* and *Lake Bonneville*
179 will only be used when referring to the entire lake cycle, encompassing all fluctuations depicted
180 in Figs 1A, B; earlier major lake cycles in these basins exist and have other names (Oviatt et al.,
181 1999).

182

183 We note that there are differences in the degree of certainty in the different lake level
184 reconstructions. For example, it is thought that the timing of the Bonneville lake stage is much
185 better constrained than the end of the overflowing phase at the Provo shoreline (Oviatt, 2015).
186 In the case for Lake Lahontan, different interpretations of sediment cores and outcrops have
187 also led to conflicting lake level reconstructions (Reheis et al., 2014). Despite these nuances,
188 our experimental design requires that we take the interpreted lake level curves at face value.
189 We use the lake level histories by Oviatt (2015) and Benson et al. (2013) for Lake Bonneville
190 and Lake Lahontan, respectively, to constrain the temporal evolution of the lake load in our
191 model, one of the key initializing inputs in our workflow (Fig. S1). In each iteration, we update
192 the lake level curve such that it coincides with the shoreline feature elevations on the modeled
193 paleotopography (see Section 3.1 and Fig. S1). Lastly, we test the sensitivity of our results to
194 the timing of the end of the Provo lake stage.

195

196 2.2 Shoreline data

197 We use elevation data of shoreline features from three sources: Adams et al. (1999), which
198 provides data for the Seho shoreline of Lake Lahontan; Currey (1982) for both the Bonneville
199 and Provo stages of Lake Bonneville; and Chen and Maloof (2017) for the Bonneville stage of
200 Lake Bonneville. We note that an important part of the study carried out by Chen and Maloof
201 (2017) was a revisitation of the Bonneville shoreline feature data collected by Currey (1982).
202 Because Currey (1982) carried his study out prior to GPS availability, approximately half of his

203 sites were remeasured with modern differential GPS technology (Chen & Maloof, 2017).
204 Therefore, while we use the Currey (1982) dataset of Provo shoreline features in its entirety, we
205 combine both datasets by Currey (1982) and Chen and Maloof (2017) for our analysis of
206 Bonneville shoreline features, opting to use revisited measurements by Chen and Maloof (2017)
207 when available. In total, these datasets provide shoreline feature elevation constraints at 170
208 sites for the Seho lake stage; 274 sites for the Bonneville lake stage; and 112 sites for the
209 Provo lake stage (Fig. 1D-F).

210

211 In order to use all three datasets simultaneously, additional processing is required. First, the
212 longitude, latitude, and elevation data are converted to use the same coordinate system and
213 vertical datum: the North American Datum of 1983 (NAD 83) and the North American Vertical
214 Datum of 1988 (NAVD 88) (see Supplementary Material, SM, for details). Second, we address
215 potential biases introduced by differences in the tools and methods used to measure shoreline
216 feature elevations. While all the data by Adams et al. (1999) and Chen and Maloof (2017) were
217 in-field measurements made by total station survey and GPS, the data by Currey (1982) have
218 been shown to generally overestimate the elevation of features (by 1.8 ± 1.4 m, on average)
219 (Chen and Maloof, 2017). Therefore, we apply an adjustment to the data by Currey (1982)
220 based on the method used for each site (see SM for details). Third, we address potential biases
221 introduced by different shoreline feature types in each dataset. Along a shoreline of a lake,
222 many processes associated with the same body of water can form adjacent shoreline features
223 with differing morphological characteristics. Such features include spits, barrier ridges, pocket
224 barriers, wave-cut terraces, and incised alluvial fans (e.g., Adams and Wesnousky, 1998; Chen
225 and Maloof, 2017). Because we require solid earth deformation patterns as captured by
226 shoreline features that record the position of the mean formative water surface (the *still water*
227 *level*; SWL), we must consider differences in how this surface is manifested by each type of
228 shoreline feature. To account for such differences we implement a scheme similar to that of

229 Chen and Maloof (2017) to determine SWL constraints from elevational measurements of
230 shoreline features gathered by Currey (1982) and Adams et al. (1999) (see SM for details).
231

232 Because we are solely interested in understanding the deformation pattern induced by lake
233 rebound and a possible regional tilt, we also remove from our analysis shoreline features which
234 are known to have, or are strongly suspected of having, undergone a non-negligible amount of
235 local, post-depositional displacement by other processes. Examples of such excluded data
236 include shoreline features associated with the Wasatch Fault flanking the eastern boundary of
237 Lake Bonneville, and localities associated with Pahvant Butte or Cove Creek Dome that have
238 undergone volcanic deformation since the Holocene (see SM for details, Fig. 1E).

239

240 **3. Viscoelastic model**

241 We calculate the deformational and gravitational response to Pleistocene lake and ice loads
242 globally using a spectral approach with spherically symmetric Maxwell rheology (Peltier, 1974).
243 Previous work employed a half-space geometry and did not account for gravitational effects
244 (Bills et al., 2007; Bills et al., 1994).

245

246 3.1 Lake rebound modeling

247 Calculating the response of the solid Earth to changes in the pluvial lakes requires inputs of
248 Earth's internal viscoelastic structure and the temporal evolution of the lake load. We perform a
249 suite of calculations in which we vary the elastic thickness of the lithosphere and sub-
250 lithospheric viscosity. It is important to note that the elastic thickness of the lithosphere, as
251 utilized here, is a quantity that can differ from lithospheric thickness estimates obtained from
252 seismology or geochemistry (Watts et al., 2013). In our calculations, the lithosphere is treated
253 as a completely elastic solid, while an underlying mantle that is treated viscoelastically.

254

255 The lake volume could be estimated using the elevation of the lake shoreline (Fig. 1A, B) and
256 the present-day topography. However, this approach underestimates the lake volume because it
257 neglects the downward deflection of the lake basin when the lake load was present. For
258 example, for Lake Bonneville, the lake volume would be underestimated by nearly 20% (Fig.
259 S2C). Thus, estimates of paleolake volumes and lake level curves are dependent on the spatial
260 pattern and magnitude of lake rebound, and vice versa. To avoid this circularity, we iteratively
261 calculate the lake volume, self-consistently accounting for the deflection of the solid Earth and
262 its gravity field (Fig. S1).

263

264 We begin with an initial estimate of the lake volume that we derive by filling the present-day
265 topography following a given lake level curve (Figs. 1A, B). We use present-day topography
266 from ETOPO1 (Amante and Eakins, 2009) (approx. 1.8 km spatial resolution). Next, we step
267 through time, calculating the gravitational and deformational response to this changing load for
268 a given viscoelastic Earth structure (Peltier, 1974). We do not assume isostatic equilibrium at
269 each timestep but account for the full time-dependent viscoelastic and gravitational response.
270 Since this signal is smooth, this calculation can be performed at a coarser resolution (*ca.* 20
271 km). The resulting time-varying topographic change is linearly interpolated onto a grid of higher
272 resolution and combined with present-day topography to obtain a time-dependent,
273 reconstructed, high-resolution paleotopography.

274

275 The adjusted topography, together with the lake level curve, is then used to re-calculate the
276 time-dependent lake volume. This new lake volume is once more used to calculate the solid
277 Earth response. We iterate over this procedure until the solid Earth response and the lake
278 volume remain unchanged for any further iteration. In each iteration, we aim to verify that the
279 prescribed lake level curve fills the lake up to the observed SWL (and not higher or lower)
280 during the Seho, Bonneville, and Provo lake stage. To accomplish this goal, we include one

281 additional step in each iteration. After the deflection due to lake loading is calculated, we
282 determine the adjusted elevation of the observed SWL on the new paleotopography. For
283 example, if SWL is inferred to be at 1550 m at a certain location today and loading deflected this
284 site down to 1530 m, the adjusted elevation of SWL corrected for deformation is 1530 m. We
285 next update the lake level curve to fill the lake up to the mean adjusted elevation of all SWL data
286 points during the lake stages for which we have observations (Sehoo, Bonneville, and Provo).
287 This iterative procedure results in the three self-consistently calculated quantities: (1)
288 reconstructed paleotopography, (2) lake level histories and (3) lake volumes for both Lakes
289 Bonneville and Lahontan (Fig. S2).

290

291 3.2 Ice age modeling

292 In order to calculate the response of the solid Earth to the changing Laurentide ice sheet, we
293 use a gravitationally self-consistent approach to solve the sea level equation (Kendall et al.,
294 2005). This approach takes the redistribution of water between ice and oceans into account and
295 accurately captures the migration of coastal shorelines and changes in Earth's rotation axis. We
296 use three ice models for our ice load: ICE-6G (Peltier et al., 2015), the LW-6 ANU ice model
297 (Lambeck et al., 2017) and NAICE (Gowan et al., 2016). For ICE-6G, we remove mountain
298 glaciers in the western U.S. because their size in this ice model is significantly larger than actual
299 reconstructions of glacier sizes derived from moraine studies (Fig. S3, Table S1 and references
300 therein).

301

302 All ice models are based on different sets of relative sea level curves from around the ice sheet
303 and GPS observations of present-day solid Earth deformation. The ANU and NAICE models
304 further use proglacial lake levels as constraints in their reconstruction. The ICE-6G and NAICE
305 models use a fixed Earth viscosity model and invert for the ice evolution, while the ANU model
306 jointly inverts for ice and Earth parameters. The ICE-6G and ANU models consider the

307 requirement of matching the LGM sea level lowstand and adjust the ice evolution without explicit
308 ice physics requirements. In contrast, the NAICE model does not attempt to match the large
309 LGM ice mass needed to match the LGM sea level lowstand, but does employ a physical ice
310 sheet model to determine the shape of the ice sheet.

311

312 As a result of the wide variety of constraints adopted, the ice models vary significantly. Notably,
313 the ICE-6G ice sheet has the largest volume overall and the ICE-6G and ANU ice models have
314 large ice domes over Hudson Bay, which is absent in the NAICE model (Fig. 3). The ice volume
315 in the region just north of the western U.S. (red square in Fig. 3C) is also largest in the ICE-6G
316 model and similar in size between the ANU and NAICE model (Fig. 3D). Furthermore, their
317 temporal evolutions differ. Both the ICE-6G and ANU ice models reach their maximum extent
318 early (26 ka), which is related to fitting the LGM sea level lowstand, while the NAICE model
319 exhibits a later maximum ice extent around 19 ka, during which ice mass in the southwestern
320 Laurentide exceeds that of the ANU ice model. The main ice retreat in the NAICE model occurs
321 after 17 ka, while it is later in the ANU and ICE-6G model (after 14.5 ka).

322

323 We pair each ice model with different models of Earth's internal viscoelastic structure and
324 compare the resulting shape of the peripheral bulge to the lake rebound corrected shoreline
325 elevations. The formation and collapse of the Laurentide ice sheet's peripheral bulge itself also
326 affects the spatial distribution of the lake load described in Section 3.1. Therefore, we must
327 perform an additional suite of iterative lake rebound calculations in which we include this ice age
328 deflection in the time-dependent paleotopography that is used to self-consistently calculate the
329 lake volume (Section 3.1, Fig. S1).

330

331

332 **4. Results and Discussion**

333

334 4.1 Deflection due to lake rebound

335 We investigate the fit between the reconstructed SWL and the predicted lake rebound that is
 336 obtained using the algorithm outlined in Section 3.1. For the Earth model, we vary the elastic
 337 thickness of the lithosphere from 10 km to 30 km and explore sub-lithospheric viscosities
 338 spanning a range of 5×10^{18} to 5×10^{19} Pa s, guided by earlier inversions (Bills et al., 2007; Bills
 339 et al., 1994). The lake rebound pattern will only be sensitive to shallow mantle structure given
 340 the limited lateral extent of the lake. We used perturbation theory to calculate the viscosity
 341 sensitivity kernel (Lau et al., 2016) and found that for a reference model with a 25km thick
 342 elastic lithosphere and 10^{19} Pa s a upper mantle viscosity, the sensitivity of the lake rebound
 343 induced surface deflection rapidly decreases below 300km. We therefore choose the sub-
 344 lithospheric viscosity to extend to 300 km depth, and fix the viscosity structure beneath to that of
 345 the standard VM5 viscosity profile (Peltier et al., 2015). For the elastic and density structure, we
 346 assume PREM (Dziewonski and Anderson, 1981).

347

348 To evaluate the misfit between our predictions and the observations, we use the reduced chi-
 349 squared metric, χ_{red}^2 :

$$350 \quad \chi_{red}^2 = \frac{1}{n-m} \cdot \sum_{i=1}^n \frac{(o_i - p_i)^2}{\sigma_i^2} \quad (1)$$

351

352 where n is the number of observations, m is the number of fitted parameters, p_i and o_i are the i -
 353 th predicted and observed SWL, respectively, and σ_i is the latter's uncertainty. The smaller this
 354 metric, the better the fit, however, once χ_{red}^2 is 1, the fit is as good as would be expected given
 355 the uncertainties in the observations. We will report the number of fitted parameters (m) that we
 356 use in each calculation throughout the study.

357

358 We find that the best fitting Earth model is not the same between the different lakes (Fig. 4).
359 While the Seho and Bonneville lake stages are most consistent with an elastic thickness of 20–
360 25 km and a low viscosity ($< 2 \times 10^{19}$ Pa s), best fits for the Provo lake stage are obtained for a
361 slightly thinner elastic thickness (15–20 km) and a stiffer underlying mantle ($> 3 \times 10^{19}$ Pa s).
362 The higher misfits at low viscosities for the Provo lake stage are due to an underprediction of
363 the magnitude of rebound. A larger magnitude can be obtained if the lake at the Provo lake
364 stage is not in isostatic equilibrium but instead still experiences remnant deformation from the
365 larger magnitude Bonneville deformation. Therefore, the discrepancy between the Bonneville
366 and Provo shorelines can be reduced if the Provo lake stage formed earlier than 15 ka.
367 Sensitivity tests demonstrate that the region of best fit is pushed towards weaker viscosities for
368 earlier times of formation (Fig. S4). If the Provo shoreline features formed 1,000 years earlier
369 (16 ka), the best-fitting Bonneville and Provo lake stage viscoelastic models would be more
370 consistent. This earlier time of formation is within the data uncertainty of the Provo shoreline
371 (Oviatt, 2015). Another possible explanation for this discrepancy is that a two-parameter Earth
372 model is not sufficient to capture the deformation of the shoreline. Repeating our analysis with
373 the viscosity profile by Bills et al. (1994), which uses a 9-layer viscosity profile (including the
374 lithosphere) that was inverted for using similar shoreline elevations, results in χ_{red}^2 values of
375 0.62, 11.5, and 3.0 ($m = 9$) for Seho, Bonneville, and Provo lake stages, respectively. Note that
376 the χ_{red}^2 for the Bonneville lake stage is higher due to the lower data uncertainty. With exception
377 to the Provo lake stage, these χ_{red}^2 values are higher than those obtained using our best fitting
378 viscosity structures (χ_{red}^2 of 0.61, 10.2, and 3.3 ($m = 2$) for Seho, Bonneville, and Provo lake
379 stages, respectively; viscosity structure marked by white box in Fig. 4).
380
381 In the remainder of this study, we will use a model with an elastic lithospheric thickness of 20
382 km and a sublithospheric viscosity of 2×10^{19} Pa s (white box in Fig. 4), which reasonably

383 captures the rebounds of Lake Lahontan and Lake Bonneville (Fig. 5). We infer a volume of
384 $10,250 \text{ km}^3$ and $4,920 \text{ km}^3$ for the Bonneville and Provo lake stage, respectively (Fig. S2C),
385 which is in agreement with the Bonneville volume estimates made by Chen and Maloof (2017),
386 but slightly smaller than estimates by Adams and Bills (2016) who obtained $10,420 \text{ km}^3$ and
387 $5,290 \text{ km}^3$ for the Bonneville and Provo lake stage, respectively. The volume for the Seho lake
388 stage is 2.0 km^3 (Fig. S2F), which is slightly smaller than the value of 2.2 km^3 used by Bills et al.
389 (2007) that is based on shoreline elevations from Benson et al. (1995).

390

391 To investigate any remaining residual deflection in the shoreline data, we remove the predicted
392 lake rebound pattern from the observations (Fig. 6A-C). We find a noticeable north-south trend
393 in the residual shoreline data, tilted down towards north (Fig. 6D-F). We employ the Mann-
394 Kendall test to investigate whether there is a monotonic (upward or downward) trend in the data
395 that significantly differs from zero (Kendall and Gibbons, 1990). For all three lakes, the results of
396 the Mann-Kendall test indicate that there is a north-south trend to a 99.9% level of significance.

397

398 4.2 Deflection due to ice peripheral forebulge

399 Next, we test the hypothesis that the trends detected in the lake rebound corrected shoreline
400 observations (Fig. 6D-F) are caused by the long wavelength deformation associated with the
401 Laurentide ice sheet. We perform a suite of ice age calculations following the method described
402 in Section 3.2. These model predictions will be sensitive to the evolution of the Laurentide ice
403 sheet and viscosities at greater depth compared to the lake rebound given the larger spatial
404 extent of the Laurentide ice sheet. We explore three ice models (ICE-6G, ANU, and NAICE) and
405 a suite of mantle viscosities. To maintain a fit to the lake rebound patterns, we construct
406 viscosity profiles that follow our best fit model from Section 4.2 (20 km elastic lithospheric
407 thickness and $2 \times 10^{19} \text{ Pa s}$ sublithospheric viscosity) and vary the viscosity between 300 km
408 and the base of the transition zone (670 km) from 10^{20} Pa s to 10^{21} Pa s and the viscosity

409 between the base of the transition zone and 1175 km depth from 5×10^{20} Pa s to 5×10^{21} Pa s
410 (grey shaded bands in Fig. 7). Each ice model is associated with a specific viscosity profile (Fig.
411 7), which mostly represents mantle structure underneath the Canadian shield. We deviate from
412 these profiles here in order to investigate Earth structure underneath the western U.S. and pair
413 each ice model with different models of Earth's internal viscoelastic structure.

414

415 Ideally we would like to perform calculations with lateral viscosity variations. However, these
416 calculations are computationally expensive and not well suited to explore the parameter space.
417 We therefore perform calculations with radially symmetric viscosity structures that allow running
418 many ice—viscosity scenarios. However, this approach comes at the expense that viscosity
419 profiles are global and, in this case, incorrect in locations such as for example Hudson Bay. In
420 light of this, we perform one additional calculation with lateral variations in viscosity to explore
421 this model limitation (see SM).

422

423 Once more, we determine χ_{red}^2 between the observations and predictions, which now includes
424 both the prediction for lake rebound and ice peripheral forebulge deformation. In the lake
425 rebound calculation, we now include the ice age tilt in our paleotopography, causing slight
426 movement of the water load towards the southern part of the lake that modifies the loading. To
427 test whether the fit to the data is significantly improved when a modeled ice age tilt is included,
428 we use a two-sample *F*-test. This test assesses the degree to which the variance in the lake
429 rebound corrected observations is distinct from the variance in the observations that are
430 corrected for both the lake rebound and the ice age tilt, accounting for uncertainty in the
431 observations.

432

433 4.2.1 Trends in viscosity

434 Modeling results show that the higher the viscosity (in parts of the upper or lower mantle), the
435 larger the predicted tilt across the forebulge. Increasing viscosity in the parts of the upper and
436 lower mantle that we vary here leads to a higher viscosity contrast across 300km depth and 670
437 km depth, both of which results in flow that is more localized at shallow depth, leading to a
438 steeper peripheral bulge. The sensitivity to the ice age tilt is largest for the Bonneville lake stage
439 (Fig. 8B, E, H). At high viscosities, the ice age tilt that is predicted is larger than the lake
440 rebound corrected elevations, leading to an increase in χ_{red}^2 compared to no ice age tilt
441 correction (purple color, Fig. 8). However, at lower viscosities, the ice age tilt is flatter and
442 results in a good fit to the observed tilt in the lake rebound corrected shoreline observations
443 (green color, Fig. 8). For the Bonneville lake stage, the F -test reveals that the spread of the
444 residuals is significantly improved when low viscosity Earth models are adopted (Fig. 8B, E,
445 solid line 90% significance level; dashed line 85% significance level). The χ_{red}^2 metric shows
446 that for the Seho and Provo lake stages, the fit improves for most viscosity structures when the
447 ice age tilt is considered (especially Fig. 8A, C, D, F), but the spread of the residuals is not
448 significantly reduced (note how no areas are outlined by a black solid or dashed line).

449

450 4.2.2 Trends across ice sheet reconstructions

451 For the ICE-6G ice model, tilt predictions for the Bonneville lake stage match the lake rebound
452 corrected observations for low viscosities in the parts of the upper and lower mantle that are
453 varied here, with trade-offs between the two (black outline, Fig. 8B). The ANU ice model does
454 not lead to a significant reduction in the variability of residuals (at 90% significance) for the
455 Bonneville lake stage, which indicates that, for our viscosity range, this ice model does not
456 capture the tilt as well as the other ice models. Overall, the χ_{red}^2 values vary less between runs
457 for the ANU model, which suggests that the sensitivity to viscosity variations is lower for this ice
458 model. The NAICE model leads to similar results compared to ICE-6G, despite the significant

459 differences in the ice history (Fig. 8B, H). For the Bonneville lake stage, tilt predictions match
460 the lake rebound corrected observations best for low viscosities in the parts of the upper and
461 lower mantle varied here, with trade-offs between the two (black outline, Fig. 8H). Lastly, this ice
462 model shows most sensitivity to the Seho and Provo shorelines because it results in the
463 largest peripheral bulge for high viscosities.

464

465 The ICE-6G ice model has significantly more ice volume than the other ice models, which leads
466 to a larger peripheral bulge (Figs. S5A). However, more ice volume also results in stronger
467 gravitational attraction, counteracting the tilt in the paleoshorelines caused by peripheral bulge
468 deformation (Fig. 2B, Fig. S5B). Considering the Bonneville lake stage, ICE-6G results in a
469 large peripheral bulge that is only somewhat compensated by the self-gravitation effect of the
470 ice sheet, causing a significant tilt across the lake (Fig. S5C). The smaller NAICE ice model on
471 the other hand leads to a smaller peripheral bulge, but also less self-gravitation resulting in the
472 preservation of the tilt signal across the lake (Fig. S5G-I). In the ANU ice model, the ice
473 distribution in the western Laurentide ice sheet is significantly smaller than the eastern
474 Laurentide ice sheet (Fig. 3B). As a consequence, the peripheral bulge is centered on South
475 Dakota to the northeast of Lake Bonneville rather than directly north as is the case for ICE-6G
476 and NAICE (Fig. S5D-F). Therefore the ANU ice model leads to slightly less sensitivity to the
477 specific viscosity profile and a worse fit to the clear north-south trend in the residuals.

478

479 Considering the lake stages at 15 ka, the NAICE model leads to the largest peripheral bulge,
480 despite significantly less ice volume than the other ice models (Fig. 3D). This result can be
481 explained by the interplay of forebulge deformation and self-gravity of the ice sheet. In the
482 NAICE ice model, the ice sheet retreats rapidly after 17 ka associated with the collapse of the
483 Laurentide-Cordilleran Ice Sheet saddle. In response to this retreat, the peripheral bulge slowly
484 subsides, leading to a peripheral bulge at 15 ka that is smaller than the one in both ICE-6G and

485 ANU, but still significant. The loss of self-gravitation associated with the ice sheet is, in contrast,
486 instantaneous, and thus no longer counteracts the deformation associated with the peripheral
487 bulge. The combined result is that NAICE exhibits the largest tilt signal among the three ice
488 models (Fig. S6).

489

490 4.2.3 Discussion of preferred ice-Earth model

491 The best fitting ice-Earth model (lowest overall χ_{red}^2) is the NAICE ice sheet model paired with a
492 viscosity of 2.5×10^{20} Pa s between 300 – 670km depth and 5×10^{20} Pa s below that (white
493 rectangle, Fig. 8H). A direct comparison between the lake rebound corrected shorelines and the
494 ice age tilt from this model shows good agreement (Fig. 9). As described in Section 3.2, this
495 calculation includes a recalculation of the lake rebound that takes the ice age deformation (solid
496 Earth tilt and gravitational effects) into account, which causes the distribution of the water load
497 to shift southward. This adjustment leads to less rebound in the northern part of the lake and
498 slightly more rebound in the southern part, resulting in deformed contours within the lake (Fig.
499 9A–C). Overall this process acts to slightly decrease the inferred water volume for Lake
500 Bonneville resulting in a volume of 10,187 km³ and 4,893 km³ for the Bonneville and Provo lake
501 stage, respectively. After the correction for the ice age tilt, there is no longer a significant north-
502 south trend in the corrected observations (Fig. 9D-F, significance level 95%). Using our iterative
503 approach to calculating the lake rebound and tilt corrected paleotopography, we provide gridded
504 datasets of reconstructed water depth for the Seho, Bonneville, and Provo lakes (see SM, Fig.
505 S7).

506

507 Our best fitting Earth structure models have viscosities that are low relative to a Laurentide-
508 centered viscosity model throughout the mantle (Fig. 7). However, trade-offs exist and may
509 allow for higher viscosities in the lower mantle, which would require an even lower viscosity in
510 the upper mantle between 300 – 670km depth. The low viscosity throughout the upper and

511 lower mantle and the corresponding muted deformation of the peripheral bulge is consistent
512 with sea level indicators along the U.S. West Coast (Creveling et al., 2017). A low viscosity
513 across the upper mantle also has been found for far-field sea level sites (Lambeck et al., 2017)
514 and underneath the Amundsen Sea (Barletta et al., 2018). However, at greater depths (>400
515 km), seismic tomography suggests the presence of slab fragments associated with multiple
516 stages of subduction (Sigloch, 2011), which would be expected to result in higher viscosities
517 compared to what is found here.

518

519 4.2.4 Limitations of this analysis

520 There are several limitations to our results. First, our results are non-unique and trade-offs exist
521 in the viscosity model and the ice sheet reconstruction. It is likely that including additional,
522 potentially high viscosity intermediate layers interspersed with lower viscosity layers could
523 produce an equally good fit to the observed ice age tilt. Trade-offs also exist in the ice sheet
524 reconstruction regarding the size of the ice sheet, the time of ice growth and the spatial
525 distribution.

526

527 Second, while the observations derived from the lake rebound process represent a local
528 constraint on subsurface viscosity structure, the ice age tilt has sensitivity to viscosity structure
529 that extends to depth (as explored here) as well as laterally, towards the former ice sheet
530 (Crawford et al., 2018). We explore this sensitivity with one additional exploratory simulation
531 (see SM, Figs S8 and S9) and find that lateral variations in viscosity can affect the direction of
532 the peripheral bulge tilt. Particularly we find that low viscosities associated with the Yellowstone
533 hotspot can lead to a northeast-southwest tilt in the prediction. While this trend is not evident in
534 the data, when combined with the ANU ice model it could lead to a more north-south trending
535 forebulge. These results are very sensitive to the specific shape and magnitude of lateral
536 viscosity variations, which remain poorly understood. Exploring these, paired with a variety of

537 ice models, requires more efficient inversion schemes for models with lateral variability in Earth
538 structure, which are currently being developed (Crawford et al., 2018).

539

540 4.3 Remaining patterns in shoreline elevations

541 While the ice age tilt can explain a significant portion of the lake rebound corrected elevations,
542 systematic residuals persist (Fig. 10). The χ_{red}^2 parameter is below 1 for the Seho lake stage,
543 which suggests that the shoreline elevations can be explained by our two modeled processes,
544 within observational uncertainty. By contrast, χ_{red}^2 remains above 1 for Lake Bonneville,
545 indicating that additional mechanisms of post depositional deformation are required to explain
546 the spread in the data. Particularly, there is an additional east-west trending pattern in the lake
547 rebound and ice age tilt corrected shoreline elevations of Lake Bonneville (Fig. 10A, B). The
548 eastern flank of Lake Bonneville is bordered by the Wasatch fault, which has been active since
549 the formation of the paleolake shorelines (USGS, 2017) and vertical displacements since the
550 Holocene are on the order of meters (DuRoss, 2008). Additional parallel faults exist that have
551 experienced less displacement (Fig. 10C) (Friedrich et al., 2003). The pattern of low residuals
552 on the WSW and ENE side, and high residuals in a NNW-SSE strip down the middle could be
553 associated with NNW trending tilted fault blocks or a cylindrical fold associated with continuing
554 tectonic activity on the Wasatch and parallel faults. A comparison of the residuals to the
555 locations of deltaic depocenters (Currey, 1982) and glacial ice caps (Laabs and Munroe, 2016)
556 that might have caused additional deformation does not reveal any obvious spatial relationship
557 (Fig. 10C).

558

559 **5. Conclusions**

560 We revisit the deformed elevational pattern of Lake Bonneville and Lake Lahontan shoreline
561 features to investigate the different contributions to their deformation. The first order signal is the
562 unloading of these extinct lakes, which leads to a domal deformation pattern in the lake

563 shorelines. In line with previous work, we find that the degree of lake rebound is indicative of a
564 thin elastic lithosphere and weak upper mantle, consistent with the wider tectonic context of this
565 region. Upon correction for lake rebound, we find that the residual shorelines show a systematic
566 and statistically significant northward dipping trend, a pattern that is consistent with a regional tilt
567 induced by the peripheral bulge created by the extinct Laurentide ice sheet. We perform a suite
568 of ice age calculations and find that the fit to the shoreline data is improved when we include the
569 loading and associated deformation of the Laurentide ice sheet. We explore what ice sheet
570 reconstructions and viscosity profiles produce the best fit to the observed shorelines. We find
571 that while ice volume is a primary control on the size of the peripheral bulge, this effect is
572 counter-acted by self-gravity of the ice sheet, resulting in a good fit between the rebound
573 corrected shoreline observations and the predicted tilt for both large (ICE-6G) and small
574 (NAICE) ice sheets. However, the ice distribution affects the size and orientation of the
575 peripheral bulge and we find that an ice model with most of its ice volume in the eastern
576 Laurentide (ANU) is less compatible with the rebound corrected shoreline observations. Lateral
577 variations in Earth's viscoelastic structure can also affect the orientation of the peripheral bulge
578 and might counteract this misfit. Largely independent of the ice sheet model, we find that the tilt
579 is only obtained when the viscosity profile exhibits low viscosities relative to Laurentide centered
580 estimates, which could occur in the upper or lower mantle. Since this result is consistent across
581 the different ice models, it supports the emerging notion that lateral variations in Earth's internal
582 properties are significant and must be considered in global sea level studies (Li et al., 2018).
583 Remaining residuals likely are related to tectonic deformation with possible implications for
584 seismic hazard assessment.

585

586 **Author contributions**

587 JA led the experimental design of the work, implemented the model simulations, and directed
588 the analysis and interpretation of results, with input from CYC, HL, and ACM. CYC and ACM

589 initiated the project. CYC gathered and reassessed the observational data, with input from JA.
590 KL ran the 3D finite volume model simulations, with input from JA. JA led the drafting of the
591 figures and manuscript text; CYC contributed text regarding the observational data. All authors
592 made significant contributions to the editing of the manuscript.

593

594 **Acknowledgements**

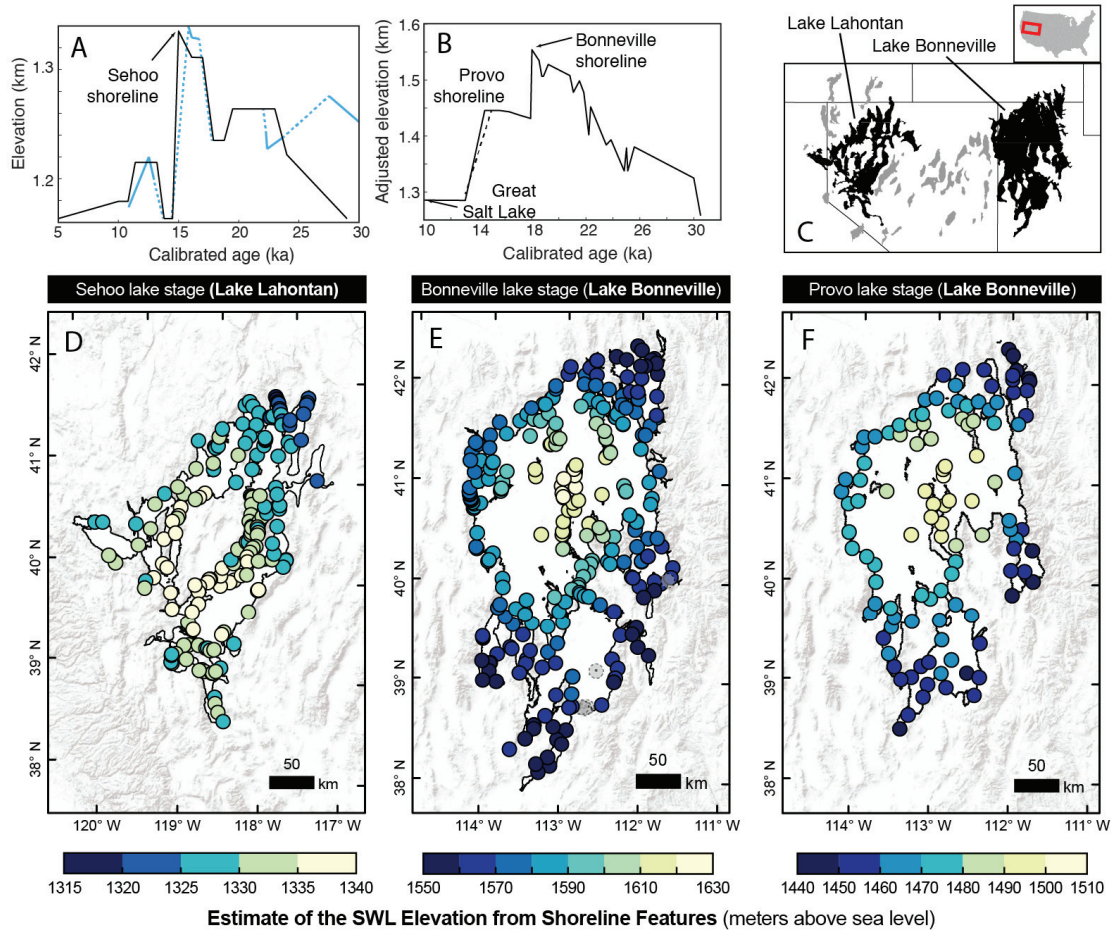
595 CYC acknowledges support from a National Science Foundation Graduate Research
596 Fellowship. CYC and ACM would like to thank Jeroen Tromp, Hom Nath Gharti, and Aaron
597 Putnam for their role in conceiving and developing an earlier version of this project carried out
598 for CYC's undergraduate senior thesis in 2012-2013. CYC would also like to thank Ken Adams,
599 Bruce Bills, and Jack Oviatt for their generous and helpful discussions during the Lake
600 Bonneville Geologic Conference in October 2018. JA would like to thank Evan Gowan for input
601 on the ice sheet models. HL acknowledges support from that Harvard Society of Fellows. We
602 thank the anonymous reviewer for their contribution to the peer review of this work. We
603 acknowledge computing resources from Columbia University's Shared Research Computing
604 Facility project, which is supported by NIH Research Facility Improvement Grant
605 1G20RR030893-01, and associated funds from the New York State Empire State Development,
606 Division of Science Technology and Innovation (NYSTAR) Contract C090171, both awarded
607 April 15, 2010.

608

609

610 **Figures**

611 **Figure 1: Lake level chronology and shoreline elevations for Lake Lahontan and Lake**
 612 **Bonneville.** A, B) Reconstruction of lake level curve for Lake Lahontan (black curve from
 613 Benson et al., 2013, which is used here; light blue curve from Reheis et al., 2014) and Lake
 614 Bonneville (Oviatt, 2015). For Lake Bonneville, the elevation has been adjusted to account for
 615 the rebound of the shoreline (Oviatt, 2015). We extended the Provo stage until 14 ka to test
 616 different timings for the duration of the Provo shoreline (dashed line indicates original
 617 reconstruction by Oviatt (2015); solid line indicates the curve used here). C) Geographic setting
 618 of Lake Lahontan and Lake Bonneville. D-F) Reconstructed still water level (SWL) from the
 619 Seho, Bonneville, and Provo shoreline features, respectively. Reconstructions are based on
 620 the original data by Adams et al. (1999); Chen and Maloof (2017); Currey (1982). Points that
 621 have been removed due to other deformation processes are shown as transparent markers with
 622 dashed outline.



623

624 **Figure 2: Schematic effect of Laurentide ice sheet on Western U.S. lakes. A)**

625 Reconstruction of relative topography at 18 ka based on the ICE-6G VM5 ice and Earth model

626 (Peltier et al., 2015). The thick grey line indicates the outline of the ice sheet at 18 ka. Lake

627 Lahontan (west) and Lake Bonneville (east) are shown with a black outline, positioned roughly

628 at 40°N. B) Schematic illustration of the effect of the Laurentide ice sheet on paleolakes in the

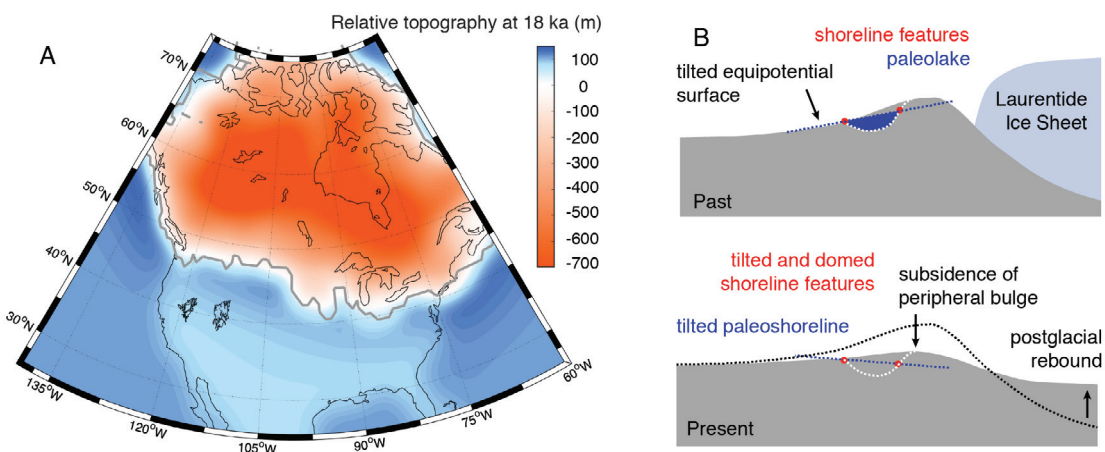
629 western U.S. Paleoshorelines of lakes on the distal side of the peripheral bulge are predicted to

630 dip down towards the ice sheet today. This is a result of the combined effects of solid Earth

631 deformation, which leads to a downward dip, and a changing gravitational pull of the Laurentide

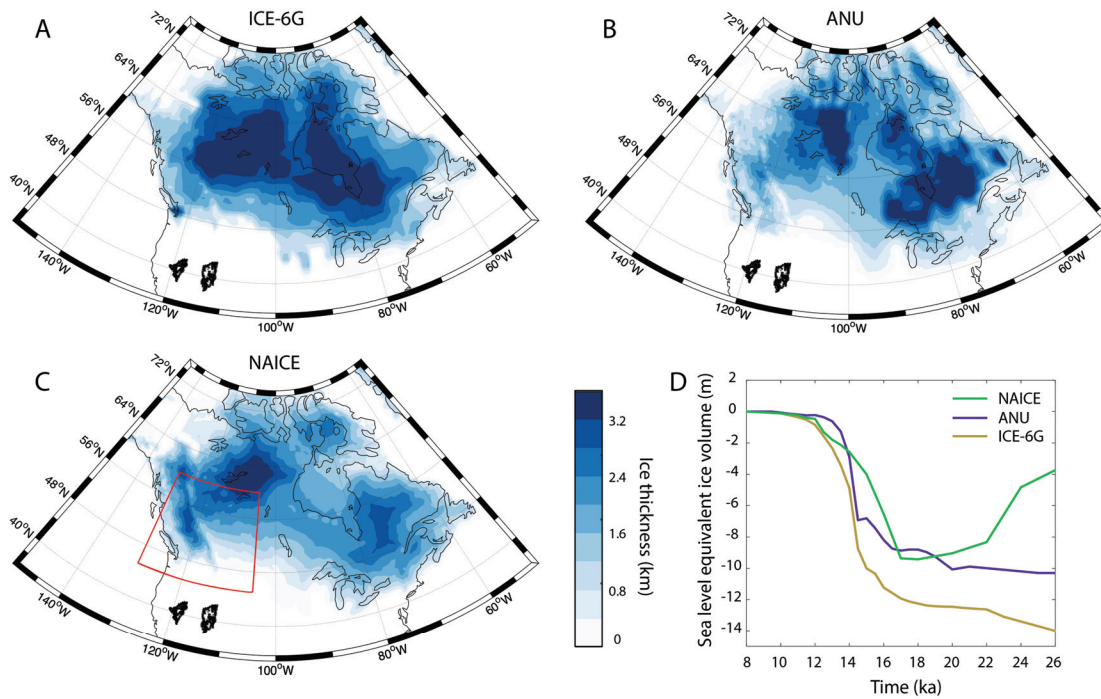
632 ice sheet, which acts to reduce the total downward dip.

633



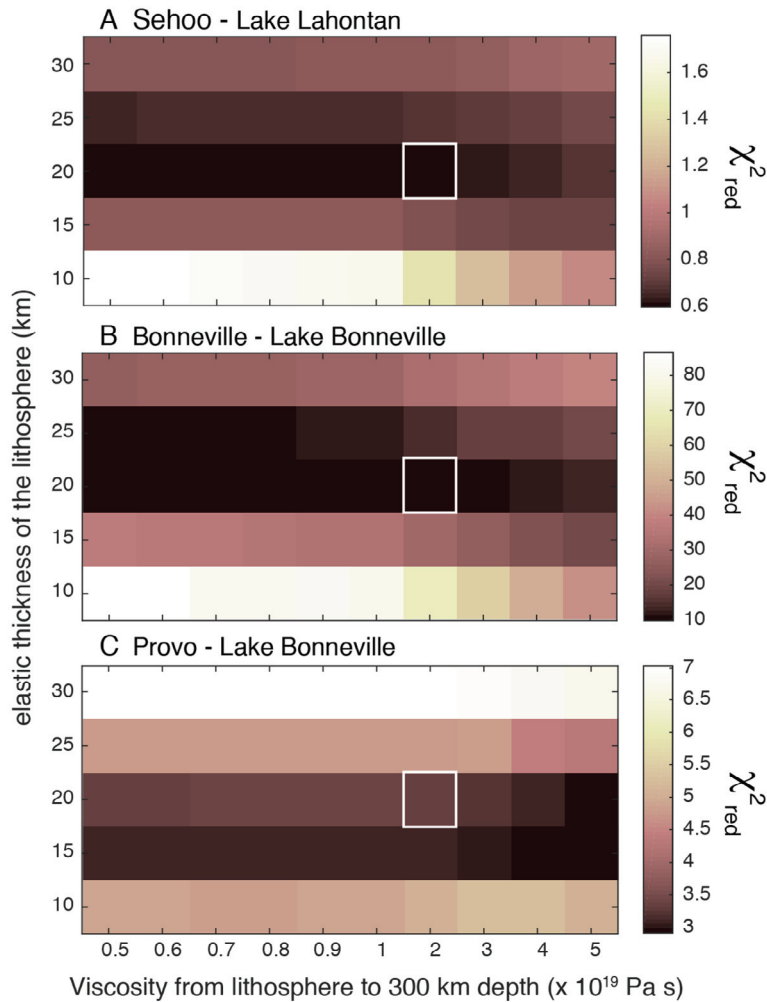
634

635 **Figure 3: Different ice sheet models.** A-C) Ice sheet thickness at 18 ka from ice model ICE-
 636 6G (Peltier et al., 2015), the ANU ice model (Lambeck et al., 2017) and NAICE (Gowan et al.,
 637 2016), respectively. D) Sea level equivalent ice volume during the deglaciation for the
 638 southwestern part of the Laurentide ice sheet (red box in panel C) during the deglaciation.
 639



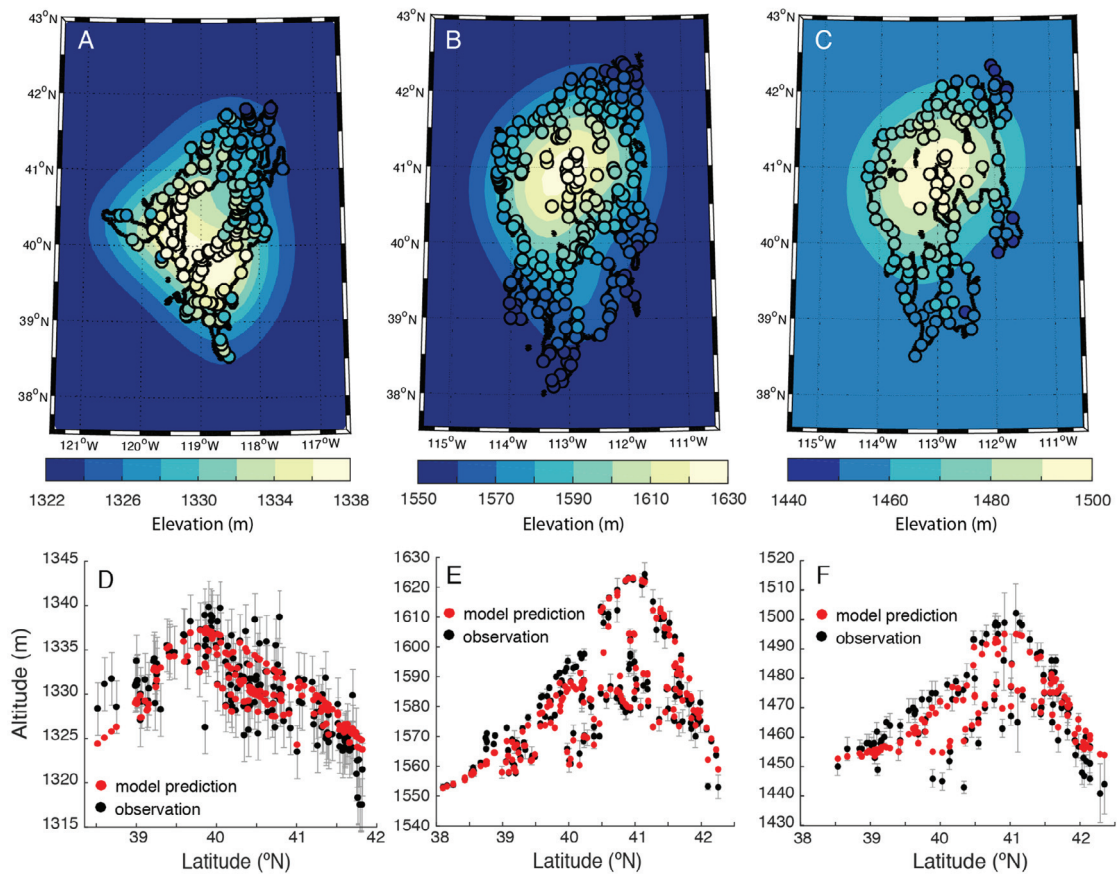
640

641 **Figure 4: Constraints on Earth structure based on lake rebound.** Misfit between the
 642 predicted SWL and the observed SWL for different Earth models with varying thickness of the
 643 elastic lithosphere (vertical axis) and sublithospheric viscosity (horizontal axis). The viscosity
 644 below 300 km follows VM5 (Peltier et al., 2015). Panels A, B, and C show results for the Seho,
 645 Bonneville, and Provo lake stages, respectively. The misfit is quantified as the reduced chi-
 646 squared value (i.e., χ_{red}^2 ; Eq. 1 with $m=2$). The white box indicates the model parameters we
 647 use for the rest of this study.



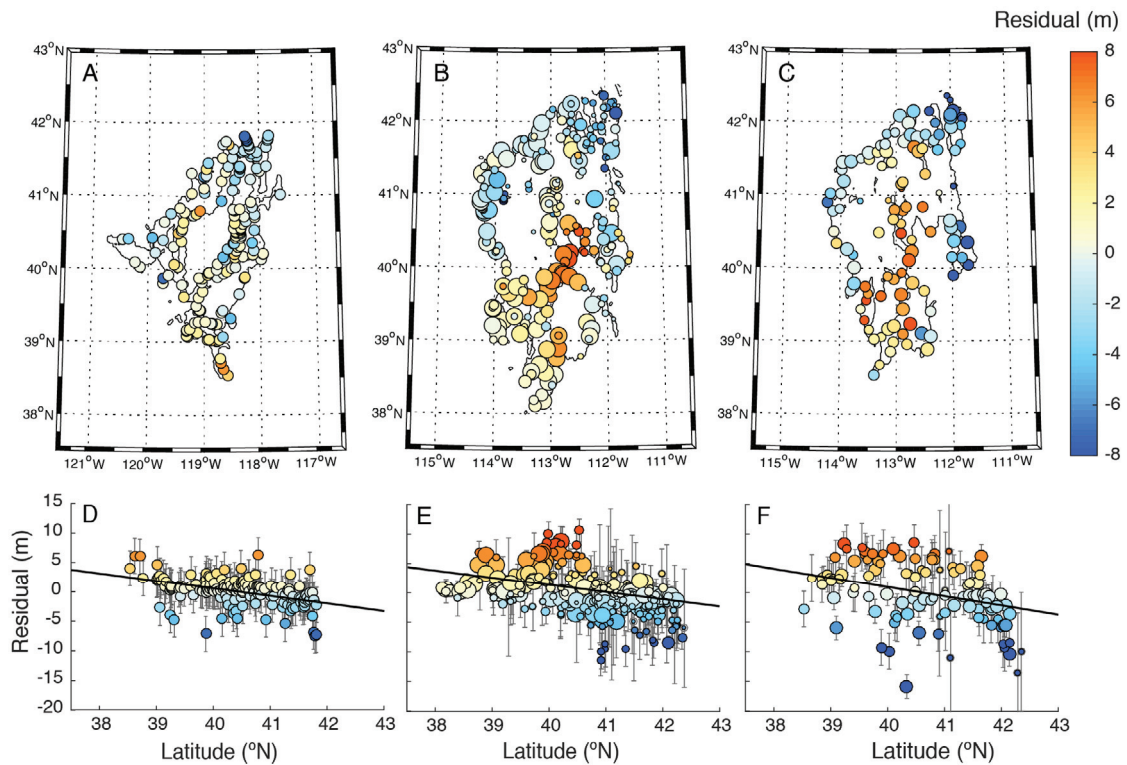
648

649 **Figure 5: Data-model comparison for lake rebound.** Comparison between the predicted SWL
 650 and the observed SWL for our preferred Earth model (white box in Fig. 4). Panels A, B, and C
 651 show results for the Seho, Bonneville, and Provo lake stages, respectively. Underlying
 652 contours show the model prediction while overlain circles show the data. Panels D, E, and F
 653 show this comparison as a function of latitude. Black markers are observations and their
 654 associated uncertainties, red markers are the model prediction. Error bars represent 1-sigma
 655 range uncertainties for SWL estimates.



656

657 **Figure 6: Residual elevations after lake rebound has been corrected for.** Data minus
 658 prediction for the same Earth model as in Fig. 5. Panels A, B, and C show results for the Seho,
 659 Bonneville, and Provo lake stages, respectively. Panels D, E, and F show the residuals as a
 660 function of latitude which reveal a clear northward dipping trend. A best fitting trendline
 661 (accounting for elevation uncertainty) is shown by the black line. The marker sizes in all panels
 662 are inversely proportional to the data uncertainty. Uncertainties are scaled the same in panel D
 663 and F, but are different in panel E (applying the same scaling would lead to very large markers).

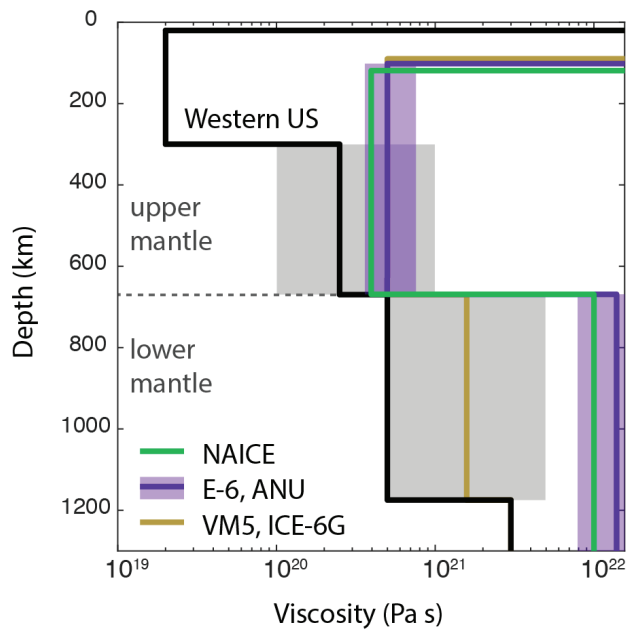


664

665

666

667 **Figure 7: Viscosity profiles.** Profiles that are associated with the different ice models are
 668 shown in color. Note that the E-6 ANU model in purple is the best-fitting Earth model for the ice
 669 model LW-6 used here and is provided with an uncertainty. The grey bands indicate the range
 670 over which we varied the viscosity. Only certain viscosity profiles are permitted by the tilt in the
 671 Bonneville shorelines (see Fig. 8). The black viscosity profile corresponds to one of the best
 672 fitting profiles for the western U.S. based on fitting the tilt in the lake rebound corrected paleo
 673 shorelines (this viscosity model is outlined by a white box in Fig. 8).

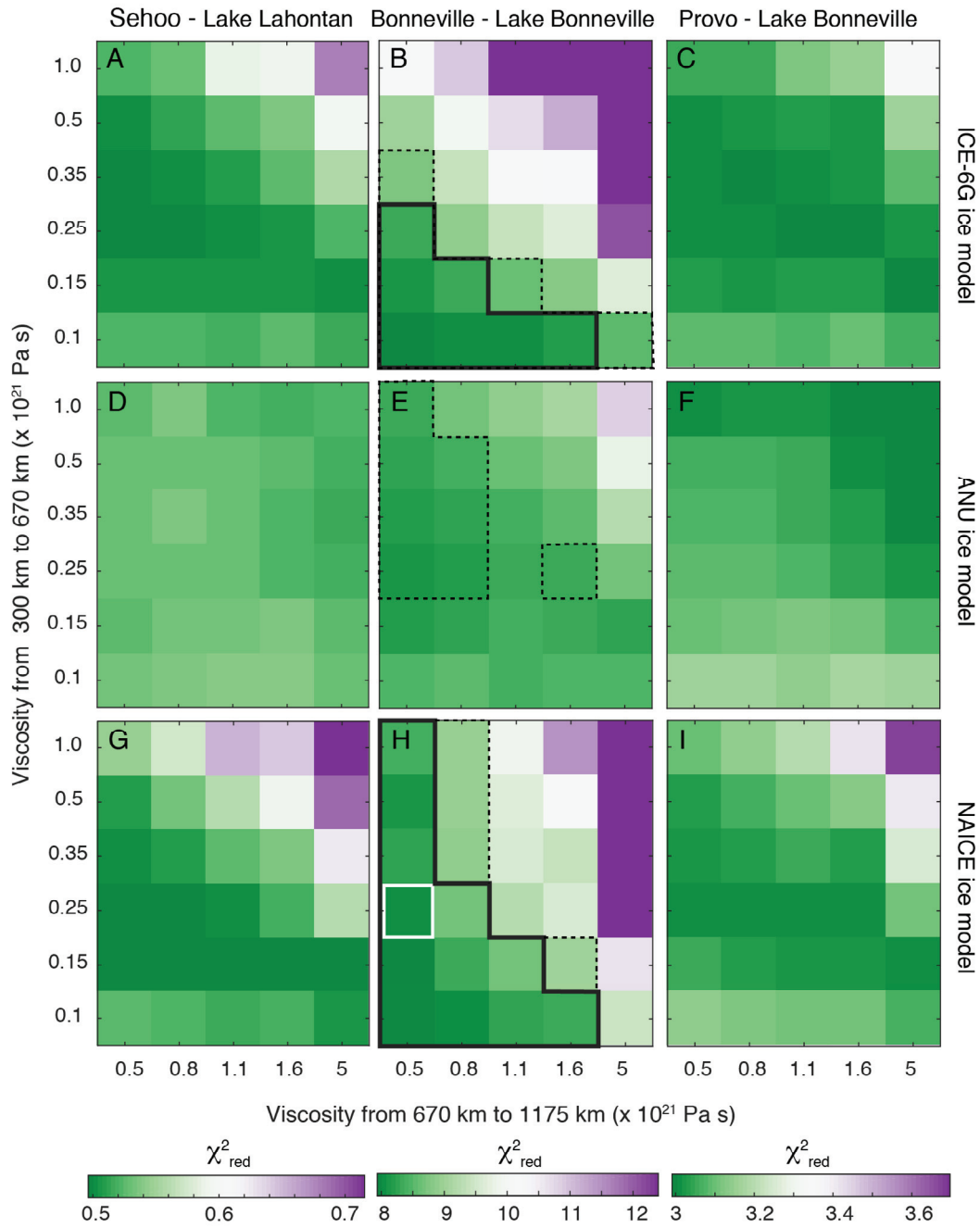


674

675

676

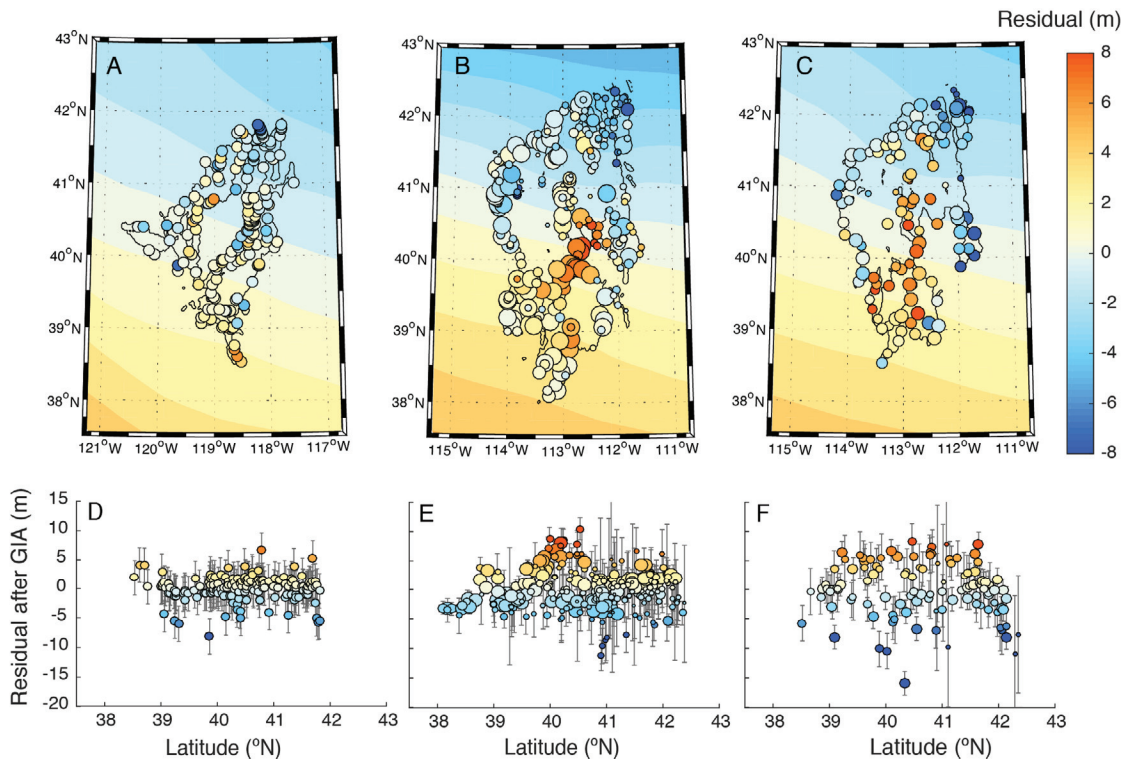
677 **Figure 8: Constraints on the peripheral bulge.** Misfit between the residuals (SWL corrected
678 for lake rebound) and the ice age tilt calculated from different ice and Earth models. Panels A-C,
679 D-F, G-I show results for the ICE-6G, ANU, and NAICE ice model, respectively. Left, middle,
680 and right panels show results for the Seho, Bonneville, and Provo lake stages, respectively.
681 The viscosity structure varies in parts of the upper mantle (between a depth range of 300-670
682 km, vertical axis) and lower mantle (between a depth range of 670-1175 km, horizontal axis).
683 Above 300 km the Earth structure is identical to what is used in Figs. 5 and 6. The viscosity
684 below 1175 km is 3×10^{21} Pa s. The misfit is quantified as χ_{red}^2 (Eq. 1 with $m = 4$) and the color
685 scale is centered on the χ_{red}^2 value obtained without a correction for the ice age tilt. Purple
686 colors indicate that the fit is worse when the ice age tilt is accounted for, green colors show that
687 the fit improves. Tiles outlined in black indicate runs that show a significant improvement when
688 the ice age tilt is corrected for (based on the F -test, solid line is 90% significance level, dashed
689 line shows 85% significance level). The white box indicates the model parameters used in Figs
690 9 and 10 and shown by the black line in Fig. 7.



691

692

693 **Figure 9: Data-model comparison of the ice age signal.** Comparison between the residuals
 694 (SWL corrected for lake rebound) and prediction from ice age calculation for the viscosity model
 695 shown outlined in white in Fig. 8. Panels A, B, and C show results for the Seho, Bonneville,
 696 and Provo lake stages, respectively. Underlying contours show the model prediction, while
 697 circles show the observations. Note the deflection of contours within the lake that arise from
 698 additional lake loading when the ice age tilt is accounted for in the lake rebound calculation.
 699 Panels D - F, show the residuals after correction for the ice age signal as a function of latitude.
 700 Marker sizes in all panels are inversely proportional to the data uncertainty. Uncertainties are
 701 scaled the same in panel D and F, but are different in panel E (applying the same scaling would
 702 lead to very large markers).



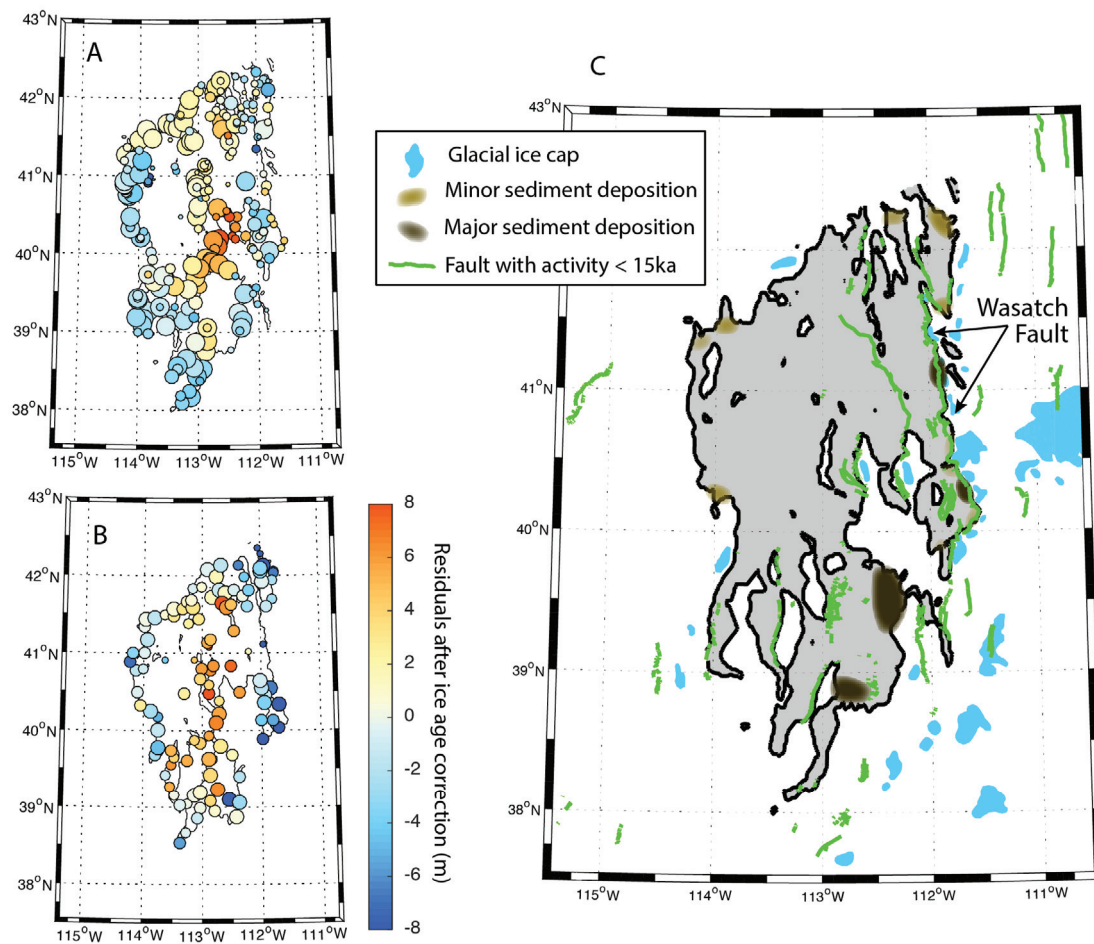
703

704

705

706

707 **Figure 10: Remaining signal in shoreline elevations.** A, B) Residuals after correction for ice
 708 age tilt for the Bonneville and Provo lake stage, respectively. Panel C shows other potential
 709 drivers for post depositional deformation within the Lake Bonneville vicinity. Fault locations are
 710 from USGS (2017), glacial ice caps from Laabs and Munroe (2016), and sediment depocenters
 711 from Currey (1982).



712

713

714 **References**

- 715 Adams, K.D., Bills, B.G., 2016. Isostatic Rebound and Palinspastic Restoration of the
716 Bonneville and Provo Shorelines in the Bonneville Basin, UT, NV, and ID, Lake Bonneville - A
717 Scientific Update, pp. 145-164.
- 718 Adams, K.D., Wesnousky, S.G., 1998. Shoreline processes and the age of the Lake
719 Lahontan highstand in the Jessup embayment, Nevada. *Geological Society of America Bulletin*
720 110, 1318-1332.
- 721 Adams, K.D., Wesnousky, S.G., Bills, B.G., 1999. Isostatic rebound, active faulting, and
722 potential geomorphic effects in the Lake Lahontan basin, Nevada and California. *Geological*
723 *Society of America Bulletin* 111, 1739-1756.
- 724 Amante, C., Eakins, B.W., 2009. ETOPO1 1 Arc-Minute Global Relief Model:
725 Procedures, Data Sources and Analysis. NOAA Technical Memorandum NESDIS NGDC-24.
726 National Geophysical Data Center, NOAA.
- 727 Barletta, V.R., Bevis, M., Smith, B.E., Wilson, T., Brown, A., Bordoni, A., Willis, M.,
728 Khan, S.A., Rovira-Navarro, M., Dalziel, I., Smalley, R., Jr., Kendrick, E., Konfal, S., Caccamise,
729 D.J., 2nd, Aster, R.C., Nyblade, A., Wiens, D.A., 2018. Observed rapid bedrock uplift in
730 Amundsen Sea Embayment promotes ice-sheet stability. *Science* 360, 1335-1339.
- 731 Benson, L., Kashgarian, M., Rubin, M., 1995. Carbonate deposition, Pyramid Lake
732 subbasin, Nevada: 2. Lake levels and polar jet stream positions reconstructed from radiocarbon
733 ages and elevations of carbonates (tufas) deposited in the Lahontan basin. *Palaeogeography,*
734 *Palaeoclimatology, Palaeoecology* 117, 1-30.
- 735 Benson, L.V., Currey, D.R., Dorn, R.I., Lajoie, K.R., Oviatt, C.G., Robinson, S.W., Smith,
736 G.I., Stine, S., 1990. Chronology of expansion and contraction of four great Basin lake systems
737 during the past 35,000 years. *Palaeogeography, Palaeoclimatology, Palaeoecology* 78, 241-
738 286.
- 739 Benson, L.V., Smoot, J.P., Lund, S.P., Mensing, S.A., Foit, F.F., Rye, R.O., 2013.
740 Insights from a synthesis of old and new climate-proxy data from the Pyramid and Winnemucca
741 lake basins for the period 48 to 11.5 cal ka. *Quaternary International* 310, 62-82.
- 742 Bills, B.G., Adams, K.D., Wesnousky, S.G., 2007. Viscosity structure of the crust and
743 upper mantle in western Nevada from isostatic rebound patterns of the late Pleistocene Lake
744 Lahontan high shoreline. *Journal of Geophysical Research* 112.
- 745 Bills, B.G., Currey, D.R., Marshall, G.A., 1994. Viscosity estimates for the crust and
746 upper mantle from patterns of lacustrine shoreline deformation in the Eastern Great Basin.
747 *Journal of Geophysical Research: Solid Earth* 99, 22059-22086.

- 748 Bills, B.G., May, G.M., 1987. Lake Bonneville: Constraints on lithospheric thickness and
749 upper mantle viscosity from isostatic warping of Bonneville, Provo, and Gilbert stage shorelines.
750 *Journal of Geophysical Research: Solid Earth* 92, 11493-11508.
- 751 Briggs, R.W., Wesnousky, S.G., Adams, K.D., 2005. Late Pleistocene and Late
752 Holocene Lake Highstands in the Pyramid Lake Subbasin of Lake Lahontan, Nevada, USA.
753 *Quaternary Research* 64, 257-263.
- 754 Cathles, L.M., 1975. *The Viscosity of the Earth's Mantle*. Princeton University Press,
755 Princeton, N.J., p. 386.
- 756 Chen, C.Y., Maloof, A.C., 2017. Revisiting the deformed high shoreline of Lake
757 Bonneville. *Quaternary Science Reviews* 159, 169-189.
- 758 Crawford, O., Al-Attar, D., Tromp, J., Mitrovica, J.X., Austermann, J., Lau, H.C.P., 2018.
759 Quantifying the sensitivity of post-glacial sea level change to laterally varying viscosity.
760 *Geophysical Journal International* 214, 1324-1363.
- 761 Creveling, J.R., Mitrovica, J.X., Clark, P.U., Waelbroeck, C., Pico, T., 2017. Predicted
762 bounds on peak global mean sea level during marine isotope stages 5a and 5c. *Quaternary*
763 *Science Reviews* 163, 193-208.
- 764 Crittenden, M.D., 1963. Effective viscosity of the Earth derived from isostatic loading of
765 Pleistocene Lake Bonneville. *Journal of Geophysical Research* 68, 5517-5530.
- 766 Currey, D.R., 1982. *Lake Bonneville: Selected features of relevance to neotectonic*
767 *analysis*. Open-File Report 82-1070, U.S. Geological Survey,, p. 31.
- 768 Dickinson, H., Freed, A.M., Andronicos, C., 2016. Inference of the viscosity structure and
769 mantle conditions beneath the Central Nevada Seismic Belt from combined postseismic and
770 lake unloading studies. *Geochemistry, Geophysics, Geosystems* 17, 1740-1757.
- 771 DuRoss, C.B., 2008. Holocene Vertical Displacement on the Central Segments of the
772 Wasatch Fault Zone, Utah. *Bulletin of the Seismological Society of America* 98, 2918-2933.
- 773 Dziewonski, A.M., Anderson, D.L., 1981. Preliminary reference Earth model. *Physics of*
774 *the Earth and Planetary Interiors* 25, 297-356.
- 775 Friedrich, A.M., Wernicke, B.P., Niemi, N.A., Bennett, R.A., Davis, J.L., 2003.
776 Comparison of geodetic and geologic data from the Wasatch region, Utah, and implications for
777 the spectral character of Earth deformation at periods of 10 to 10 million years. *Journal of*
778 *Geophysical Research: Solid Earth* 108.
- 779 Gilbert, G.K., 1885. *The Inculcation of Scientific Method by Example, with an illustration*
780 *drawn from the Quaternary Geology of Utah*. *Am. J. Sci.* 3, 284-299.

- 781 Gowan, E.J., Tregoning, P., Purcell, A., Montillet, J.-P., McClusky, S., 2016. A model of
782 the western Laurentide Ice Sheet, using observations of glacial isostatic adjustment. *Quaternary*
783 *Science Reviews* 139, 1-16.
- 784 Iwasaki, T., Matsu'ura, M., 1982. Quasi-static crustal deformations due to a surface load:
785 Rheological structure of the earth's crust and upper mantle. *Journal of Physics of the Earth* 30,
786 469-508.
- 787 Kendall, M.G., Gibbons, J.D., 1990. *Rank Correlation Methods*, Oxford University Press.
- 788 Kendall, R.A., Mitrovica, J.X., Milne, G.A., 2005. On post-glacial sea level - II. Numerical
789 formulation and comparative results on spherically symmetric models. *Geophysical Journal*
790 *International* 161, 679-706.
- 791 Laabs, B.J.C., Munroe, J.S., 2016. Late Pleistocene Mountain Glaciation in the Lake
792 Bonneville Basin, Lake Bonneville - A Scientific Update, pp. 462-503.
- 793 Lambeck, K., Purcell, A., Zhao, S., 2017. The North American Late Wisconsin ice sheet
794 and mantle viscosity from glacial rebound analyses. *Quaternary Science Reviews* 158, 172-210.
- 795 Lau, H.C.P., Austermann, J., Mitrovica, J.X., Crawford, O., Al-Attar, D., Latychev, K.,
796 2018. Inferences of Mantle Viscosity Based on Ice Age Data Sets: The Bias in Radial Viscosity
797 Profiles Due to the Neglect of Laterally Heterogeneous Viscosity Structure. *Journal of*
798 *Geophysical Research: Solid Earth* 123, 7237-7252.
- 799 Lau, H.C.P., Mitrovica, J.X., Austermann, J., Crawford, O., Al-Attar, D., Latychev, K.,
800 2016. Inferences of mantle viscosity based on ice age data sets: Radial structure. *Journal of*
801 *Geophysical Research: Solid Earth* 121, 6991-7012.
- 802 Lekić, V., Fischer, K.M., 2014. Contrasting lithospheric signatures across the western
803 United States revealed by Sp receiver functions. *Earth and Planetary Science Letters* 402, 90-
804 98.
- 805 Li, T., Wu, P., Steffen, H., Wang, H., 2018. In search of laterally heterogeneous viscosity
806 models of glacial isostatic adjustment with the ICE-6G_C global ice history model. *Geophysical*
807 *Journal International* 214, 1191-1205.
- 808 Mifflin, M.D., Wheat, M.M., 1971. Isostatic rebound in the Lahontan basin, northwestern
809 Great Basin, *Geol. Soc. Am. Abstr.* 7: 647.
- 810 Miller, D.M., Oviatt, C.G., McGeehin, J.P., 2013. Stratigraphy and chronology of Provo
811 shoreline deposits and lake-level implications, Late Pleistocene Lake Bonneville, eastern Great
812 Basin, USA. *Boreas* 42, 342-361.

- 813 Nakiboglu, S.M., Lambeck, K., 1982. A study of the Earth's response to surface loading
814 with application to Lake Bonneville. *Geophysical Journal of the Royal Astronomical Society* 70,
815 577-620.
- 816 Oviatt, C.G., 1997. Lake Bonneville fluctuations and global climate change. *Geology* 25.
- 817 Oviatt, C.G., 2015. Chronology of Lake Bonneville, 30,000 to 10,000 yr B.P. *Quaternary*
818 *Science Reviews* 110, 166-171.
- 819 Oviatt, C.G., Currey, D.R., Sack, D., 1992. Radiocarbon chronology of Lake Bonneville,
820 Eastern Great Basin, USA. *Palaeogeography, Palaeoclimatology, Palaeoecology* 99, 225-241.
- 821 Oviatt, C.G., Jewell, P.W., 2016. The Bonneville Shoreline, Lake Bonneville - A Scientific
822 Update, pp. 88-104.
- 823 Oviatt, C.G., Thompson, R.S., Kaufman, D.S., Bright, J., Forester, R.M., 1999.
824 Reinterpretation of the Burmester Core, Bonneville Basin, Utah. *Quaternary Research* 52, 180-
825 184.
- 826 Passey, Q.R., 1981. Upper mantle viscosity derived from the difference in rebound of the
827 Provo and Bonneville Shorelines: Lake Bonneville Basin, Utah. *Journal of Geophysical*
828 *Research* 86.
- 829 Patrickson, S.J., Sack, D., Brunelle, A.R., Moser, K.A., 2010. Late Pleistocene to early
830 Holocene lake level and paleoclimate insights from Stansbury Island, Bonneville basin, Utah.
831 *Quaternary Research* 73, 237-246.
- 832 Peltier, W.R., 1974. The impulse response of a Maxwell Earth. *Reviews of Geophysics*
833 12.
- 834 Peltier, W.R., Argus, D.F., Drummond, R., 2015. Space geodesy constrains ice age
835 terminal deglaciation: The global ICE-6G_C (VM5a) model. *Journal of Geophysical Research:*
836 *Solid Earth* 120, 450-487.
- 837 Plank, T., Forsyth, D.W., 2016. Thermal structure and melting conditions in the mantle
838 beneath the Basin and Range province from seismology and petrology. *Geochemistry,*
839 *Geophysics, Geosystems* 17, 1312-1338.
- 840 Reheis, M.C., Adams, K.D., Oviatt, C.G., Bacon, S.N., 2014. Pluvial lakes in the Great
841 Basin of the western United States—a view from the outcrop. *Quaternary Science Reviews* 97,
842 33-57.
- 843 Sack, D., 2015. The Composite Nature of the Provo Level of Lake Bonneville, Great
844 Basin, Western North America. *Quaternary Research* 52, 316-327.

- 845 Schmandt, B., Humphreys, E., 2010. Complex subduction and small-scale convection
846 revealed by body-wave tomography of the western United States upper mantle. *Earth and*
847 *Planetary Science Letters* 297, 435-445.
- 848 Sigloch, K., 2011. Mantle provinces under North America from multifrequency P-wave
849 tomography. *Geochemistry, Geophysics, Geosystems* 12, n/a-n/a.
- 850 Sonder, L.J., Jones, C.H., 1999. Western United States Extension: How the West was
851 Widened. *Annual Review of Earth and Planetary Sciences* 27, 417-462.
- 852 Spencer, J.Q.G., Oviatt, C.G., Pathak, M., Fan, Y., 2015. Testing and refining the timing
853 of hydrologic evolution during the latest Pleistocene regressive phase of Lake Bonneville.
854 *Quaternary International* 362, 139-145.
- 855 USGS, 2017. Quaternary Fault and Fold Database of the United States.
- 856 Watts, A.B., Zhong, S.J., Hunter, J., 2013. The Behavior of the Lithosphere on Seismic
857 to Geologic Timescales. *Annual Review of Earth and Planetary Sciences* 41, 443-468.
- 858 Whitehouse, P.L., 2018. Glacial isostatic adjustment modelling: historical perspectives,
859 recent advances, and future directions. *Earth Surface Dynamics* 6, 401-429.
- 860 Woodward, R.S., 1888. On the form and position of mean sea level. *United States*
861 *Geological Survey Bulletin* 48, 87-170.
862

Declaration of interests

The authors declare that they have no known competing financial interests or personal relationships that could have appeared to influence the work reported in this paper.

The authors declare the following financial interests/personal relationships which may be considered as potential competing interests: